Int. J. Solids Structures Vol. 22, No. 12, pp. 1485–1500, 1986
Printed in Great Britain.

0020-7683/86 $3.00+.00
Pergamon Journals Ltd.

PENETRATION INTO DRY POROUS ROCK†

MICHAEL J. FORRESTAL
Sandia National Laboratories, Albuquerque, NM 87185, U.S.A.

(*Received* 26 *April* 1985; *in revised form* 30 *December* 1985)

Abstract—I developed closed-form solutions for forces on projectiles that penetrated geological targets. Constitutive target description consisted of a linear hydrostat and a Mohr–Coulomb failure-criterion with a tension cutoff. Predictions from the model were in reasonably good agreement with deceleration data from full-scale field-tests into dry, tuff targets.

INTRODUCTION

Studies on projectile penetration into geological targets usually focus on the prediction and measurement of penetration depth or deceleration history. Theoretical models use solution techniques that may be grouped into three main categories: empirical equations fit to test data[1]; models that approximate the target response by one-dimensional motion using cavity-expansion methods[2]; and wave-code analyses[3]. All of these approaches have advantages and limitations which should be considered for each application.

In a recent paper, Longcope and Forrestal[4] developed cylindrical, cavity-expansion models to predict forces on conical-nosed penetrators. The cavity-expansion approximation idealizes the target as thin, independent layers normal to the penetration direction and simplifies the analysis to one-dimensional motion in the radial direction. Constitutive models are guided by triaxial, material tests on samples cored from targets used for full-scale, penetration tests. The targets are described with a linear hydrostat and a Mohr–Coulomb failure-criterion with a tension cutoff[5]. For targets that have nearly constant shear-strength with increased confining pressure (such as sea-ice)[6], we use the Tresca failure-criterion.

As shown in Fig. 1, there are usually three regions of target response: an elastic region, a region with radial cracks, and a plastic region. As the penetration velocity increases, the radially cracked region diminishes and is eliminated eventually. That is, for high enough penetration velocity, the response is elastic–plastic. Target response is calculated by solving the nonlinear, wave-propagation problem with a similarity transformation and numerical evaluation of ordinary differential equations.

Penetration deceleration-time data have been retrieved for only two rock targets [7, 8]. These targets, located at the Sandia Tonopah Test Range, Nevada, are ash-flow and welded tuffs with densities $\rho_0 = 1.62$ and 1.97 mg m^{-3}, respectively. Longcope and Forrestal[4] compare predicted and measured deceleration histories for penetration into the ash-flow target (Antelope tuff) and show reasonably good agreement. However, when applying this model to the welded tuff target (Mount Helen tuff), we discovered the model overpredicted the deceleration data. In our previous paper[4], we consider the three regions of response shown in Fig. 1; however, the elastic region is modeled as rigid. In this study, the rigid region was modeled as elastic, and deceleration predictions were in better agreement with field-test measurements. We also discovered that for slow enough penetration velocity, the shear strength of the welded-tuff target was not exceeded. For this case, there was no plastic region, and the response consisted of a radially cracked region next to the penetrator nose and an elastic region. Thus, an elastic–cracked model was derived in this paper. Lastly, this study presents very accurate, closed-form solutions derived by an iterative technique; whereas, the previous models required the numerical solution of nonlinear, differential equations. These closed-form solutions were programmed for numerical evaluations on a personal computer.

† This work was supported by the U.S. Department of Energy under contract DE-AC04-76DP00789 and the Naval Civil Engineering Laboratory, Port Hueneme, California, under contract N68305-84WR40082.

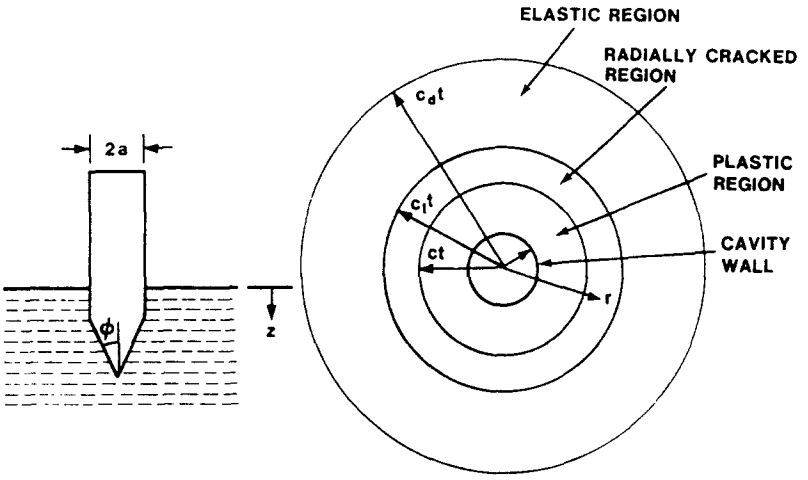

Fig. 1. Geometry and response regions.

PROBLEM FORMULATION

A rigid projectile with a conical nose penetrates a uniform target with normal incidence. As illustrated in Fig. 1, the problem is axisymmetric and further simplified by using the cylindrical, cavity-expansion approximation. The conical nose with apical angle 2ϕ expands a layer of target material and opens a cavity at constant radial velocity V, where $V = V_z \tan\phi$, and V_z is the axial penetrator velocity. This expansion usually produces three response regions: a plastic region next to the penetrator nose (the material has exceeded its shear strength); a radially cracked region (the material has exceeded its circumferential, tensile strength); and an elastic region. As discussed in the Introduction, the cracked region vanishes for fast enough penetration velocity, and the plastic region may vanish for slow enough penetration velocity.

Longcope and Forrestal show that a linear hydrostat and a linear, Mohr–Coulomb failure-criterion provide good approximations to triaxial, test data for Antelope[4] and Mount Helen[9] tuffs. Thus, the plastic region of response is described by

$$p = K(1-\rho_0/\rho) = K\eta \tag{1a}$$

$$\sigma_r - \sigma_\theta = \mu p + \tau_0; \quad \tau_0 = (1-\mu/3)Q \tag{1b}$$

$$\sigma_\theta \geq -Y \tag{1c}$$

where p is hydrostatic pressure, ρ_0, ρ are densities in the undeformed and deformed configurations; η is volumetric strain; σ_r, σ_θ are radial and circumferential stress components (positive in compression); μ, τ_0 define the failure criterion; Q is unconfined compressive strength; and Y is tensile strength. The elastic region has material constants K and Poisson's ratio ν. If a cracked region exists, it is taken as elastic with $\sigma_\theta = 0$.

The plastic region (Fig. 1) is bounded by the radii, $r = Vt$ and $r = ct$; where r is the radial, Eulerian coordinate; t is time; and c is the velocity of propagation of the plastic wave-front. Equations of mass and momentum conservation in cylindrical, Eulerian coordinates are:

$$\frac{\partial \rho}{\partial t} + \frac{1}{r}\frac{\partial}{\partial r}(r\rho v) = 0; \tag{2a}$$

$$\frac{\partial \sigma_r}{\partial r} + \frac{\sigma_r - \sigma_\theta}{r} = -\rho\left(\frac{\partial v}{\partial t} + v\frac{\partial v}{\partial r}\right); \tag{2b}$$

where v is the radial, particle velocity (positive outward). As suggested by Hill[10] and

discussed by Forrestal and Longcope[6], the axial stress is taken as $\sigma_z = (\sigma_r + \sigma_\theta)/2$. Thus, pressure becomes $p = (\sigma_r + \sigma_\theta)/2$.

The elastic and cracked regions are governed by the linear theory of elasticity. However, for the cracked region, the tensile strength has been exceeded, and $\sigma_\theta = 0$. Equations that describe the response regions are now derived.

ELASTIC–PLASTIC RESPONSE

The nonlinear equations for the plastic region are combined to eliminate σ_θ, ρ, resulting in two equations in σ_r, v:

$$\frac{\partial \sigma_r}{\partial r} + \alpha\mu\frac{\sigma_r}{r} + \frac{\alpha\tau_0}{r} = \frac{-\rho_0}{1-\eta}\left(\frac{\partial v}{\partial t} + v\frac{\partial v}{\partial r}\right) \tag{3a}$$

and

$$\frac{\partial v}{\partial r} + \frac{v}{r} = \frac{-\alpha}{K(1-\eta)}\left(\frac{\partial \sigma_r}{\partial t} + v\frac{\partial \sigma_r}{\partial r}\right), \tag{3b}$$

$$\alpha = 2/(2+\mu). \tag{3c}$$

Post-analysis numerical evaluations showed that η is small, and $(1-\eta)$ is taken as unity. The dimensionless variables

$$S = \sigma_r/K, \quad T = \tau_0/K, \quad U = v/c, \quad \varepsilon = V/c \tag{4a}$$

and the similarity transformation

$$\xi = r/ct \tag{4b}$$

are introduced. With (4a, b), eqns (3a, b) transform to

$$\xi^{-\alpha\mu}\frac{\mathrm{d}}{\mathrm{d}\xi}(\xi^{\alpha\mu}S) = \frac{-\alpha T}{\xi} + \beta^2\xi\frac{\mathrm{d}U}{\mathrm{d}\xi} - \frac{\beta^2}{2}\frac{\mathrm{d}}{\mathrm{d}\xi}(U^2), \tag{5a}$$

$$\frac{1}{\xi}\frac{\mathrm{d}}{\mathrm{d}\xi}(\xi U) = \alpha\xi\frac{\mathrm{d}S}{\mathrm{d}\xi} - \alpha U\frac{\mathrm{d}S}{\mathrm{d}\xi} \tag{5b}$$

in which

$$\beta = c/c_p, \quad c_p^2 = K/\rho_0. \tag{5c}$$

The boundary condition at the cavity wall is

$$U(\xi = \varepsilon) = \varepsilon. \tag{5d}$$

Solutions for dry, tuff targets require the Mohr–Coulomb failure-criterion; however, other targets such as sea-ice[6] or saturated sandstone[11] are modeled adequately with the Tresca criterion ($\mu = 0$). For $\mu = 0$, the solutions are less cumbersome and have different functional forms. Thus, solutions for both failure criteria are derived. For $\mu = 0$, eqns (5a, b) reduce to

$$\frac{\mathrm{d}S}{\mathrm{d}\xi} = -\frac{T}{\xi} + \beta^2\xi\frac{\mathrm{d}U}{\mathrm{d}\xi} - \frac{\beta^2}{2}\frac{\mathrm{d}}{\mathrm{d}\xi}(U^2) \tag{6a}$$

$$\frac{1}{\xi}\frac{\mathrm{d}}{\mathrm{d}\xi}(\xi U) = \xi\frac{\mathrm{d}S}{\mathrm{d}\xi} - U\frac{\mathrm{d}S}{\mathrm{d}\xi}. \tag{6b}$$

Closed-form solutions for the nonlinear eqns (5) and (6) are obtained with an iterative procedure similar to that previously used on linear equations[12]. This iterative procedure is outlined for the simpler eqns (6a, b) with $\mu = 0$. First, set the right side of (6b) to zero, solve for U, and evaluate the integration constant with (5d). This first approximation to the particle velocity is

$$U^0(\xi) = \varepsilon^2 \xi^{-1}. \tag{7a}$$

Next, substitute (7a) into the right side of (6a) and integrate. This first approximation to the radial stress is

$$S^0(\xi) = -(T+\beta^2\varepsilon^2)\ln\xi - (\beta^2\varepsilon^4/2)\xi^{-2} + B_0 \tag{7b}$$

$$B_0 = S_2 + \beta^2\varepsilon^4/2, \tag{7c}$$

where S_2 is the radial stress in the plastic region at the elastic–plastic interface, and B_0 is obtained from $S^0(\xi = 1) = S_2$.

The procedure is repeated by substituting (7a, b) into the right side of (6b), solving for U, and evaluating the intregration constant with (5d). This second approximation to the particle velocity is

$$U^1(\xi) = -(T+\beta^2\varepsilon^2)\xi/2 + \varepsilon^2(T+2\beta^2\varepsilon^2)\xi^{-1}\ln\xi + (\beta^2\varepsilon^6/2)\xi^{-3} + A_1\xi^{-1} \tag{8a}$$

$$A_1 = U_2 + (T+\beta^2\varepsilon^2)/2 - \beta^2\varepsilon^6/2, \tag{8b}$$

where U_2 is the particle velocity in the plastic region at the elastic–plastic interface and A_1 is obtained from $U^1(\xi = 1) = U_2$. As discussed by Hunter[13], the elastic–plastic interface speed c ($\beta = c/c_p$) depends on the cavity-expansion velocity V ($\beta\varepsilon = V/c_p$). This interface velocity is obtained from eqn (5d) and given by

$$1 + (T+\beta^2\varepsilon^2)/2 - (T+2\beta^2\varepsilon^2)\ln\varepsilon - \beta^2\varepsilon^2/2 - A_1\varepsilon^{-2} = 0 \tag{8c}$$

where $\beta\varepsilon = V/c_p$ is not explicitly related to $\beta = c/c_p$. As before, the second approximation to the radial stress is obtained by substituting (8a) into the right side of (6a) and integrating. Thus

$$S^1(\xi) = -[T+\beta^2 A_1 - \beta^2\varepsilon^2(T+2\beta^2\varepsilon^2)]\ln\xi - (\beta^2\varepsilon^2/2)(T+2\beta^2\varepsilon^2)(\ln\xi)^2$$
$$-(\beta^2/4)(T+\beta^2\varepsilon^2)\xi^2 + (3\beta^4\varepsilon^6/4)\xi^{-2} - (\beta^2/2)[U^1(\xi)]^2 + B_1\,; \tag{8d}$$

$$B_1 = S_2 + (\beta^2/4)(T+\beta^2\varepsilon^2) - 3\beta^4\varepsilon^6/4 + (\beta^2/2)(U_2)^2 \tag{8e}$$

where S_2 is the radial stress in the plastic region at the elastic–plastic interface and B_1 is obtained from $S^1(\xi = 1) = S_2$. It will be shown later that these iterative solutions are in excellent agreement with numerical evaluations of the nonlinear equations.

Solutions for the Mohr–Coulomb criterion are obtained with this same procedure. The first approximations are

$$U^0(\xi) = \varepsilon^2\xi^{-1}\,; \tag{9a}$$

$$S^0(\xi) = B_0\xi^{-\alpha\mu} - \left(\frac{\alpha T+\beta^2\varepsilon^2}{\alpha\mu}\right) - \left(\frac{\beta^2\varepsilon^4}{2-\alpha\mu}\right)\xi^{-2}\,; \tag{9b}$$

$$B_0 = S_2 + \left(\frac{\alpha T+\beta^2\varepsilon^2}{\alpha\mu}\right) + \frac{\beta^2\varepsilon^4}{2-\alpha\mu}. \tag{9c}$$

The second approximations are

$$U^1(\xi) = -\left(\frac{\mu\alpha^2 B_0}{2-\alpha\mu}\right)\xi^{(1-\alpha\mu)} + \left(\frac{2\alpha\beta^2\varepsilon^4}{2-\alpha\mu}\right)\xi^{-1}\ln\xi - \alpha\varepsilon^2 B_0\xi^{-(1+\alpha\mu)} + \frac{\alpha\beta^2\varepsilon^6\xi^{-3}}{(2-\alpha\mu)} + A_1\xi^{-1}\,; \tag{9d}$$

$$A_1 = U_2 + \frac{\mu\alpha^2 B_0}{(2-\alpha\mu)} + \alpha\varepsilon^2 B_0 - \frac{\alpha\beta^2\varepsilon^6}{(2-\alpha\mu)}; \tag{9e}$$

$$S^1(\xi) = S^I(\xi) + S^c(\xi) + B_1\xi^{-\alpha\mu}; \tag{9f}$$

$$S^I(\xi) = -T/\mu + \beta^2\{-(C_1/2)(1-\alpha\mu)\xi^{2-\alpha\mu} - (C_2/\alpha\mu)(\ln\xi - 1/\alpha\mu) + (C_2 - A_1)/2\mu + C_3(1+\alpha\mu)\xi^{-\alpha\mu}\ln\xi + [3C_4/(2-\alpha\mu)]\xi^{-2}\}; \tag{9g}$$

$$S^c(\xi) = \frac{-\beta^2\xi^{-\alpha\mu}}{2}\left\{\frac{6C_4^2\xi^{-6+\alpha\mu}}{(6-\alpha)} + \frac{(8C_4A_1 - 2C_2C_4)}{(4-\alpha\mu)}\xi^{-4+\alpha\mu} - \frac{(2C_2A_1 - 2A_1^2)}{(2-\alpha\mu)}\xi^{-2+\alpha\mu} + 2C_1^2(1-\alpha\mu)\xi^{2-\alpha\mu} + 4C_1C_3\xi^{-\alpha\mu} - (C_3C_4/2)(4+\alpha\mu)\xi^{-4} - [(2+\alpha\mu)(C_1C_4 + C_3A_1) + (\alpha\mu/2)C_2C_3]\xi^{-2} + \frac{2C_3^2(1+\alpha\mu)}{(2+\alpha\mu)}\xi^{-2-\alpha\mu} + [2\alpha\mu C_1A_1 - 2C_1C_2]\ln\xi + \alpha\mu C_1C_2(\ln\xi)^2 + \frac{2C_2^2(\ln\xi)^2}{(2-\alpha\mu)}\xi^{-2+\alpha\mu} + \left[4C_2A_1 + \frac{2\alpha\mu C_2^2}{(2-\alpha\mu)}\right]\left[\ln\xi + \frac{1}{(2-\alpha\mu)}\right]\frac{\xi^{-2+\alpha\mu}}{(2-\alpha\mu)} + \frac{8C_2C_4}{(4-\alpha\mu)}\left[\ln\xi + \frac{1}{(4-\alpha\mu)}\right]\xi^{-4+\alpha\mu} - C_2C_3(2+\alpha\mu)\xi^{-2}\ln\xi\right\}; \tag{9h}$$

$$B_0 = S_2 + (\alpha T + \beta^2\varepsilon^2)/(\alpha\mu) + \beta^2\varepsilon^4/(2-\alpha\mu); \tag{9i}$$

$$A_1 = U_2 + C_1 + C_3 - C_4; \tag{9j}$$

$$B_1 = S_2 - S^I(\xi = 1) - S^c(\xi = 1); \tag{9k}$$

$$C_1 = \mu\alpha^2 B_0/(2-\alpha\mu), \quad C_2 = 2\alpha\beta^2\varepsilon^4/(2-\alpha\mu); \tag{9l}$$

$$C_3 = \alpha\varepsilon^2 B_0, \quad C_4 = \alpha\beta^2\varepsilon^6/(2-\alpha\mu). \tag{9m}$$

The interface velocity $c(\beta = c/c_p)$ is related to the cavity-expansion velocity $V(\beta\varepsilon = V/c_p)$ through

$$1 + 2\alpha B_0\varepsilon^{-\alpha\mu}/(2-\alpha\mu) - \alpha\beta^2\varepsilon^2(1+2\ln\varepsilon)/(2-\alpha\mu) - A_1\varepsilon^{-2} = 0. \tag{9n}$$

It will be shown later that these iterative solutions are in excellent agreement with numerical evaluations of the nonlinear equations.

The elastic and plastic regions of response are linked through the Hugoniot jump conditions† that conserve mass and momentum across the wave-front. Written in terms of the dimensionless variables

$$U_2 = 1 - (\rho_1/\rho_2)(1 - U_1) \tag{10a}$$

$$S_2 = S_1 + \beta^2(\rho_1/\rho_0)(1 - U_1)(U_2 - U_1), \tag{10b}$$

where the subscript 2 refers to quantities in the plastic region at the wave-front, and the subscript 1 refers to quantities in the elastic region at the wave-front.

The Mohr–Coulomb or Tresca criterion (1b) holds on either side of the elastic–plastic interface. However, on the plastic side of the interface $p = (\sigma_r + \sigma_\theta)/2$, and on the elastic side $p = (\sigma_r + \sigma_\theta)(1+\nu)/3$. In terms of the dimensionless variables

$$S_2 = (1 - \rho_0/\rho_2)/\alpha + T/2 \tag{10c}$$

$$S_1 = (1 - \rho_0/\rho_1)/\alpha_e + T/2; \tag{10d}$$

† This derivation corrects errors in our previous papers[4, 6, 14]. Fortunately, these errors did not affect the numerical results.

where $\alpha_e = 2[3/(1+\nu)+\mu]^{-1}$. Eliminating ρ_1, ρ_2 from eqns (10a–d) and linearizing gives:

$$U_2 = U_1 + (\alpha - \alpha_e)(S_1 - T/2)/(1-\alpha\beta^2) \tag{11a}$$

and

$$S_2 = S_1 + \beta^2(\alpha - \alpha_e)(S_1 - T/2)/(1-\alpha\beta^2). \tag{11b}$$

Equations for the elastic response[14] are

$$S(\xi) = \frac{B\beta}{2\gamma(1-\nu)}\left\{\frac{(1-2\nu)(1-z^2)^{1/2}}{z^2} + \ln\left[\frac{1+(1-z^2)^{1/2}}{z}\right]\right\}, \quad 1 < \xi < 1/(\beta\gamma) \tag{12a}$$

$$U(\xi) = B(1-z^2)^{1/2}/z, \qquad 1 < \xi < 1/(\beta\gamma), \tag{12b}$$

in which

$$z = \beta\gamma\xi, \quad c_d = \frac{E(1-\nu)}{(1+\nu)(1-2\nu)\rho_0}, \quad \gamma^2 = \frac{(1+\nu)}{3(1-\nu)}.$$

The elastic wave-front is at $\xi = 1/\alpha$, and the elastic–plastic interface is at $\xi = 1$. The constant B is determined by satisfying the yield criterion (1b) at $\xi = 1$. Thus

$$B = \frac{T}{\dfrac{(1-2\nu)[1-(\beta\gamma)^2]^{1/2}}{(1-\nu)\beta\gamma^3} - \mu\beta\gamma\ln\left\{\dfrac{1-[1-(\beta\gamma)^2]^{1/2}}{\beta\gamma}\right\}}. \tag{12c}$$

Explicit equations for radial stress in the elastic and plastic regions are not obtainable directly from the input $V(\beta\varepsilon = V/c_p)$. However, if a value of β is chosen, the corresponding cavity-expansion velocity and radial stresses can be conveniently calculated. For a given β and specified target, material properties, $S(\xi)$ and $U(\xi)$ in the elastic region can be calculated from (12a–c). With the elastic, radial stress and particle velocity known, U_2 and S_2 are obtainable from the jump conditions (11a, b). The cavity-expansion velocity can then be calculated from (8c) for the Tresca criterion ($\mu = 0$) or from (9n) for the Mohr–Coulomb criterion. Finally, radial stress in the plastic region can be calculated from (8d, e) or (9f–m).

Laboratory experiments[15] and field tests obtain data for calculating net axial force during penetration. The axial force[16] is given by

$$F_z = \pi a^2\sigma_r(\varepsilon), \quad S(\varepsilon) = \sigma_r(\varepsilon)/K, \tag{13}$$

where a is the cylinder radius shown in Fig. 1.

ELASTIC–CRACKED–PLASTIC RESPONSE

Numerical results from the elastic–plastic model show that circumferential, tensile stresses are developed for slow penetration velocity. Since geological targets typically have a much lower, tensile than compressive strength[5], radial cracks are developed in the target. Thus, the model developed in this section contains a radially cracked region (Fig. 1) between the elastic and plastic regions. Equations for the plastic region were derived in the previous section. However, these equations require the radial stress and particle velocity in the plastic region at the cracked–plastic interface (S_2, V_2). Values of S_2, V_2 for this model are now obtained from analyses of the elastic and cracked regions.

The radially cracked region has zero circumferential-stress and is bounded by $r = ct$ and $r = c_1 t$, where c_1 is the propagation velocity of the elastic–cracked interface. Response equations for this region are obtained from the linear version of (2b) with $\sigma_\theta = 0$; and,

as assumed for the plastic region, $\sigma_z = (\sigma_r + \sigma_\theta)/2$. The material law uses (1a) with $\eta = -(\partial u/\partial r + u/r)$, which implies plane strain. The dimensionless radial stress and particle velocity are:

$$S(\xi) = \left[\frac{2(\beta/\beta_1)T/(2-\mu) - S_4}{1-\beta/\beta_1}\right]\left(\frac{1}{\xi} - 1\right) + \frac{2T}{(2-\mu)\xi}, \quad 1 < \xi < \beta_1/\beta \tag{14a}$$

$$U(\xi) = \left[\frac{2(\beta/\beta_1)T/(2-\mu) - S_4}{\beta^2(1-\beta/\beta_1)}\right]\left(\frac{1}{\xi} - \frac{\beta^2}{2}\right) - \frac{T}{2-\mu}, \quad 1 < \xi < \beta_1/\beta, \tag{14b}$$

where S_4 is the radial stress in the cracked region at the elastic–cracked interface ($\xi = c_1/c = \beta_1/\beta$). At the cracked–plastic interface ($\xi = 1$), eqn (14a) satisfies the yield criterion (1b) with $\sigma_\theta = 0$. Thus

$$S(\xi = 1) = S_1 = 2T/(2-\mu), \tag{15}$$

which is the radial stress in the cracked region at $\xi = 1$.

As previously discussed, the Hugoniot jump conditions link the response regions. For the cracked and plastic regions, $\sigma_z = p = (\sigma_r + \sigma_\theta)/2$. Thus, eqns (10a–c) and eqn (10d), with α_e set to α, tie together the cracked and plastic regions. Evaluation of these equations shows that radial stress and particle velocity are continuous across this interface, or

$$S_2 = S_1, \quad U_2 = U_1. \tag{16}$$

The elastic region is bounded by $r = c_1 t$ and $r = c_d t$ (Fig. 1). Equations for the elastic response are given by (12a, b) when B is defined as

$$B = \frac{2(1+\nu)T_1/\alpha\beta}{\dfrac{3(1-2\nu)[1-(\beta_1\gamma)^2]^{1/2}}{(\beta_1\gamma)^2} - 3\ln\left\{\dfrac{1+[1-(\beta_1\gamma)^2]^{1/2}}{\beta_1\gamma}\right\}}; \tag{17}$$

where $T_1 = Y/K$ and $\beta_1 = c_1/c_p$. For this value of B, the circumferential stress component in the elastic region at the elastic–cracked interface ($\xi = \beta_1/\beta$) is the maximum tensile strength ($\sigma_\theta = -Y$). As indicated by Goodman[5], Y is usually at least an order of magnitude less than the unconfined, compressive strength Q.

The elastic and cracked regions are connected with the Hugoniot jump conditions

$$U_4 = \beta_1/\beta - (\rho_3/\rho_4)[(\beta_1/\beta) - U_3] \tag{18a}$$

and

$$S_4 = S_3 + (\rho_3/\rho_0)\beta^2[(\beta_1/\beta) - U_3](U_4 - U_3). \tag{18b}$$

Since $p = (\sigma_r + \sigma_\theta)/2$ in the cracked region, $p = (1+\nu)(\sigma_r + \sigma_\theta)/2$ in the elastic region, $\sigma_\theta = -Y$ in the elastic region at the elastic–cracked interface, and $\sigma_\theta = 0$ in the cracked region

$$S_3 = T_1 + [3/(1+\nu)](1 - \rho_0/\rho_3) \tag{18c}$$

$$S_4 = 2(1 - \rho_0/\rho_4). \tag{18d}$$

Eliminating ρ_3, ρ_4 from eqns (18a–d), and linearizing gives

$$\beta U_4 = \beta U_3 + \frac{\beta_1}{(1-\beta_1^2/2)}\left[\frac{1}{2} - \frac{(1+\nu)}{3}\right]S_3 + \frac{\beta_1}{(1-\beta_1^2/2)}\left(\frac{1+\nu}{3}\right)T_1; \tag{19a}$$

$$S_4 = S_3 + \frac{\beta_1^2}{(1-\beta_1^2/2)}\left[\frac{1}{2} - \left(\frac{1+\nu}{3}\right)S_3\right] + \frac{\beta_1}{(1-\beta_1^2/2)}\left(\frac{1+\nu}{3}\right)T_1. \tag{19b}$$

As before, explicit solutions in terms of the input $V(\beta\varepsilon = V/c_p)$ are not obtainable. To calculate response in the three regions, choose a value of β_1 and calculate the elastic response from (12a, b) and (17). Values of βU_4 and S_4 can then be calculated from (19a, b). Radial stress and particle velocity in the cracked region at the cracked–elastic interface ($\xi = \beta_1/\beta$) can also be obtained from the equations for the cracked region (14a, b). Equating both values of βU_4 gives the expression for $\beta = c/c_p$

$$\beta = \frac{2\beta_1(\beta U_4)+2S_4}{\left(\frac{2}{2-\mu}\right)\left(\frac{2-\beta_1^2}{\beta_1}\right)T+\beta_1 S_4+2(\beta U_4)}, \tag{20}$$

where S_4, βU_4 are given by (19a, b). As previously discussed, radial stress and particle velocity are continuous across the plastic–cracked interface ($\xi = 1$), and values of U_2, S_2 can be obtained from (14a, b) with $\xi = 1$. Then all quantities required to calculate response in the plastic region are known. The input $V/c_p = \beta\varepsilon$ can be obtained from (8c) or (9n), and the radial stress can be calculated from (8d, e) or (9f–m).

ELASTIC–CRACKED RESPONSE

As discussed in the Introduction, the shear strength of the target may not be exceeded for materials with small, tensile strength and for slow penetration velocity. For this case there is no plastic region, and the response consists of a radially cracked region next to the penetrator nose and an elastic region. The cracked region is bounded by the cavity radius $r = Vt$ and $r = c_1 t$, where c_1 is the propagation velocity of the cracked–elastic interface. Since a hole is opened from zero radius, this solution requires a nonlinear analysis for the cracked region.

The equations that govern the cracked region are obtained from (1a) and (2a, b) with $\sigma_\theta = 0$. Following the previously used methods and assumptions:

$$\frac{dS}{d\xi}+\frac{S}{\xi} = \beta^2\left(\xi\frac{dU}{d\xi}-U\frac{dU}{d\xi}\right) \tag{21a}$$

$$\frac{dU}{d\xi}+\frac{U}{\xi} = \frac{\xi}{2}\frac{dS}{d\xi}-\frac{U}{2}\frac{dS}{d\xi}, \tag{21b}$$

with $\beta = c_1/c_p$. The boundary condition at the cavity wall is

$$U(\xi = \varepsilon) = \varepsilon. \tag{21c}$$

First approximations for particle velocity and radial stress are

$$U^0(\xi) = \varepsilon^2\xi^{-1} \tag{22a}$$

$$S^0(\xi) = -\beta^2\varepsilon^2-\beta^2\varepsilon^4\xi^{-2}+B_0\xi^{-1} \tag{22b}$$

$$B_0 = S_2+\beta^2\varepsilon^2(1+\varepsilon^2), \tag{22c}$$

where S_2 is the radial stress in the cracked region at the elastic–cracked interface ($\xi = 1$) and B_0 is obtained from $S(\xi = 1) = S_2$. The second approximation for particle velocity is

$$U^1(\xi) = \beta^2\varepsilon^4\xi^{-1}\ln\xi-(B_0/2)(1+\varepsilon^2\xi^{-2})+2\beta^2\varepsilon^6\xi^{-3}+A_1\xi^{-1}; \tag{23a}$$

$$A_1 = U_2+(B_0/2)(1+\varepsilon^2)-2\beta^2\varepsilon^6; \tag{23b}$$

where U_2 is the particle velocity in the cracked region at the elastic–cracked interface, and U_2 is obtained from $U^1(\xi = 1) = U_2$. The elastic–cracked interface speed $c_1(\beta = c_1/c_p)$ is

obtained from (21c) and given by

$$1-\beta^2\varepsilon^2(2+\ln\varepsilon)+B_0\varepsilon^{-1}+A_1\varepsilon^{-2}=0. \tag{24}$$

The second approximation for radial stress is

$$S^1(\xi)=\beta^2\xi^{-1}f_1(\xi)+\beta^2\xi^{-1}f_2(\xi)/2-\beta^2[U^1(\xi)]^2/2+B_1\xi^{-1}; \tag{25a}$$

$$f_1(\xi)=(2\beta^2\varepsilon^4-A_1)\xi+6\beta^2\varepsilon^6\xi^{-1}+B_0\varepsilon^2\ln\xi-\beta^2\varepsilon^4\xi\ln\xi; \tag{25b}$$

$$\begin{aligned} f_2(\xi)=\;& B_0^2\xi/4-(A_1^2+B_0\varepsilon^2/2+2\beta^4\varepsilon^8+2\beta^2\varepsilon^4A_1)\xi^{-1}\\ &+(4B_0\beta^2\varepsilon^6+2A_1B_0\varepsilon^2+\beta^2\varepsilon^6B_0/4)\xi^{-2}\\ &-(3B_0\varepsilon^4/4+12A_1\beta^2\varepsilon^6+4\beta^4\varepsilon^{10}/9)\xi^{-3}+8B_0\beta^2\varepsilon^8\xi^{-4}\\ &-20\beta^4\varepsilon^{12}\xi^{-5}-B_0A_1\ln\xi-(2\beta^4\varepsilon^8+2\beta^2\varepsilon^4A_1^*)\xi^{-1}\ln\xi\\ &+(\beta^2\varepsilon^6B_0/2)\xi^{-2}\ln\xi-(4\beta^4\varepsilon^{10}/3)\xi^{-3}\ln\xi\\ &-(\beta^2\varepsilon^4B_0/2)(\ln\xi)^2-\beta^4\varepsilon^8\xi^{-1}(\ln\xi)^2; \end{aligned} \tag{25c}$$

where B_1 is found from $S^1(\xi=1)=S_2$ and given by

$$B_1=S_2-\beta^2f_1(\xi=1)-(\beta^2/2)f_2(\xi=1)+(\beta^2/2)f_3(\xi=1). \tag{25d}$$

From the Hugoniot jump conditions (10a, b) and the previously applied procedures

$$U_2=U_1+\frac{1}{(1-\beta^2/2)}\left[\frac{1}{2}-\left(\frac{1+\nu}{3}\right)\right]S_1+\frac{1}{(1-\beta^2/2)}\left(\frac{1+\nu}{3}\right)T_1; \tag{26a}$$

$$S_2=S_1+\frac{\beta^2}{(1-\beta^2/2)}\left[\frac{1}{2}-\left(\frac{1+\nu}{3}\right)\right]S_1+\frac{\beta^2}{(1-\beta^2/2)}\left(\frac{1+\nu}{3}\right)T_1, \tag{26b}$$

where the subscripts 2 and 1 refer to quantities in the cracked and elastic regions, respectively, at the interface ($\xi=1$). These equations link the elastic and cracked regions. Equations for the elastic response are given by (12a,b) with B defined by (17). Numerical evaluations are obtained with the procedure outlined for the elastic–plastic model.

QUASI-STATIC RESPONSES

Quasi-static solutions have important physical significance for predicting projectile trajectories. As discussed by Hill[10], a finite pressure is required to open a hole from zero, initial radius. Thus, for an infinitesimal, cavity-expansion velocity V, there is a finite, radial stress on the cavity wall. For penetration applications, the projectile velocity V_z and cavity-expansion velocity V decrease with penetration depth. At the end of the penetrator trajectory, there is a sudden decrease (jump) in axial force. This phenomenon is observed in instrumented field-tests[4, 6]; where at the end of the event, the deceleration response jumps from a finite value to zero.

Previously developed methods of analysis[4, 10] were applied to obtain the quasi-static solutions for the response modes of this study. For the elastic–plastic model, the plastic region is bounded by the cavity wall ($r=a$) and the elastic–plastic interface ($r=R$). Radial stress in the plastic region is

$$\frac{\sigma_r}{K}=\frac{T}{\alpha\mu}\left(\frac{r}{R}\right)^{-\alpha\mu}-\frac{T}{\mu}, \quad \text{for } \mu\neq 0 \tag{27a}$$

$$\frac{\sigma_r}{K}=T\left[\frac{1}{2}+\ln\left(\frac{R}{r}\right)\right], \quad \text{for } \mu=0 \tag{27b}$$

where

$$\left(\frac{a}{R}\right)^2 = T\left[\frac{\alpha}{2-\alpha\mu} + \frac{(1+\nu)}{3(1-2\nu)}\right]. \tag{27c}$$

The elastic stress components are:

$$\frac{\sigma_r}{K} = \frac{T}{2}\left(\frac{R}{r}\right)^2; \quad \frac{\sigma_\theta}{K} = \frac{-T}{2}\left(\frac{R}{r}\right)^2. \tag{28}$$

For the elastic–cracked–plastic model, the plastic region is bounded by the cavity wall ($r = a$) and the cracked–plastic interface ($r = c$). The cracked–elastic interface is located at $r = R$. Radial stress in the plastic region is

$$\frac{\sigma_r}{K} = \frac{\tau_0}{\mu}\left(\frac{2+\mu}{2-\mu}\right)\left(\frac{r}{c}\right)^{-2\mu/(2+\mu)} - \frac{\tau_0}{\mu}, \quad \text{for } \mu \neq 0; \tag{29a}$$

$$\frac{\sigma_r}{K} = T\left[1 + \ln\left(\frac{c}{r}\right)\right], \quad \text{for } \mu = 0; \tag{29b}$$

$$\left(\frac{a}{c}\right)^2 = \frac{(5-4\nu)}{(3)(1-2\nu)}\left(\frac{2}{2-\mu}\right)^2\left(\frac{T}{T_1}\right)^2. \tag{29c}$$

In the cracked region

$$\frac{\sigma_r}{K} = \left(\frac{2}{2-\mu}\right)T\left(\frac{c}{r}\right) \tag{30}$$

and in the elastic region

$$\frac{\sigma_r}{K} = T_1\left(\frac{R}{r}\right)^2; \quad \frac{\sigma_\theta}{K} = -T_1\left(\frac{R}{r}\right)^2, \tag{31a}$$

$$\frac{c}{R} = \left(\frac{2-\mu}{2}\right)\left(\frac{T_1}{T}\right). \tag{31b}$$

For the elastic–cracked model, the cracked region is bounded by the cavity wall ($r = a$) and the elastic–cracked interface ($r = c$). Radial stress in the cracked region is

$$\frac{\sigma_r}{K} = T_1\left(\frac{c}{r}\right); \tag{32a}$$

$$\left(\frac{a}{c}\right)^2 = \left[\frac{(5-4\nu)}{3(1-2\nu)}\right]T_1 \tag{32b}$$

and the elastic stresses are

$$\frac{\sigma_r}{K} = T_1\left(\frac{c}{r}\right)^2; \quad \frac{\sigma_\theta}{K} = -T_1\left(\frac{c}{r}\right)^2. \tag{33}$$

For all these models, $\sigma_\theta = 0$ in the cracked region, and σ_θ in the plastic regions can be obtained from the radial stress and the yield criterion.

NUMERICAL EXAMPLES

In this section, graphical results from the response models for three targets are presented: sea-ice[6] with $\rho_0 = 0.92$ Mg m^{-3}, $K = 4.0$ GPa, $\tau_0 = 10.5$ MPa, $\mu = 0$, $\nu = 0.27$, $Y = 0.86$ MPa; Antelope tuff[4] with $\rho_0 = 1.62$ Mg m^{-3}, $K = 2.0$ GPa, $\tau_0 = 10$ MPa, $\mu = 1.0$, $\nu = 0.234$, $Y = 1.4$ MPa; and Mount Helen tuff[9] with $\rho_0 = 1.97$ Mg m^{-3}, $K = 9.52$ GPa, $\tau_0 = 50$ MPa, $\mu = 1.20$, $\nu = 0.25$, $Y = 3.30$ MPa.

As previously mentioned, the response modes depend on the cavity-expansion velocity and the target material properties. For small enough cavity-expansion velocity, the response is either elastic–cracked or elastic–cracked–plastic. The appropriate response mode for small, cavity-expansion velocity V can be determined from the quasi-static response solutions. Equation (27c) for the elastic–cracked–plastic response mode relates the location of the cavity wall ($r = a$) to the location of the cracked–plastic interface ($r = R$); thus, if $(a/R) > 1$, the response mode is elastic–cracked. As the cavity-expansion velocity increases, $\sigma_r(\xi = \varepsilon)$ also increases. From the yield criterion with $\sigma_0 = 0$, the response becomes elastic–cracked–plastic when $\sigma_r(\xi = \varepsilon)/K = 2T(2-\mu)$. As the cavity-expansion velocity continues to increase, the cracked region of response decreases. Finally, when the cracked–plastic, interface velocity c equals the elastic–cracked, interface velocity c_1 the response becomes elastic–plastic.

Figure 2 shows radial stress at the cavity wall $\sigma_r(\xi = \varepsilon)$ vs radial cavity-expansion velocity V for a sea-ice target with $\mu = 0$. For the air-dropped penetration tests into sea-ice targets conducted by Young and Keck[17], impact velocity was 160 m s^{-1}, $\tan\phi = 0.25$, and $V/c_p < 0.02$. However, recoilless guns have launched instrumented projectiles to about four times this impact velocity, so tests could be performed to about 600 m s^{-1}. In Fig. 2, $S^0(\xi = \varepsilon)$ and $S^1(\xi = \varepsilon)$ are compared with numerical solutions to the nonlinear equations for the elastic–plastic model. There is practically no difference between $S^1(\xi = \varepsilon)$ and the

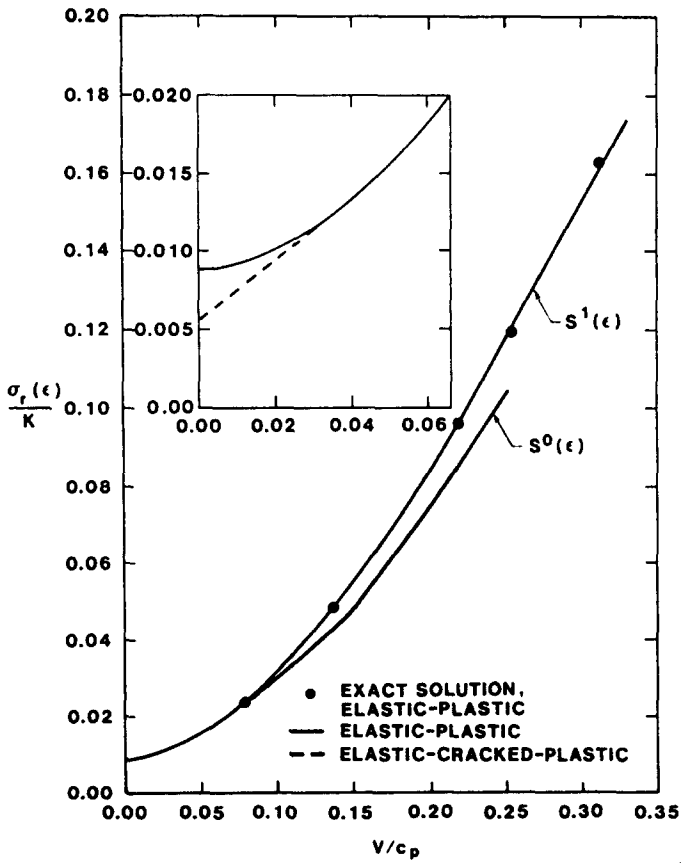

Fig. 2. Radial stress components on the conical nose for a sea-ice target. A comparison of the iterative solutions $S^0(\varepsilon)$ and $S^1(\varepsilon)$ with the exact, nonlinear solutions.

numerical, nonlinear solution for $V/c_p < 0.35$. In the upper graph, results from the elastic–cracked–plastic and elastic–plastic models are presented. For these material properties, the models predict a radially cracked region for $V/c_p < 0.04$. For $V/c_p > 0.04$, the response is elastic–plastic. In both models, the dynamic calculations gave the quasi-static values as the cavity-expansion velocity approached zero. Also, the tensile strength for this target is large enough that no cracked–elastic response mode occurred.

Figure 3 shows radial stress at the cavity wall $\sigma_r(\xi = \varepsilon)$ vs radial cavity-expansion velocity V for the Antelope tuff target. For the field test conducted by Young[8], the impact velocity was 520 m s^{-1}, and $V/c_p < 0.14$. Figure 3 compares results from the numerical, nonlinear solution with the closed-form results for the elastic–plastic response model. The dynamic calculations merge to the quasi-static values for V approaching zero, and agreement between $S^1(\xi = \varepsilon)$ and the nonlinear solution is within 9% for $V/c_p < 0.25$. At $V/c_p = 0.25$, the radial stress on the penetrator nose is $\sigma_r(\xi = \varepsilon) = 0.48$ GPa (72,000 psi) which could be a significant structural design limitation. Also, $\sigma_r(\xi = \varepsilon) = 0.48$ GPa is about the upper limit on stress magnitude for triaxial, material tests. For this target, there is a radially cracked region for $V/c_p < 0.11$, and for $V/c_p > 0.11$, the response is elastic–plastic. Tensile strength for this target is large enough that no cracked–elastic response mode occurred.

Figure 4 shows radial stress at the cavity wall $\sigma_r(\xi = \varepsilon)$ vs cavity-expansion velocity V for the Mount Helen tuff target. For the field test conducted by Patterson[7], the impact velocity was 411 m s^{-1} and $V/c_p < 0.047$. No detectable differences between $S^1(\xi = \varepsilon)$ and the nonlinear solution occur over the plotted range for this target material. Butters[18] reports $Y = 3.3$ MPa, but tensile strengths typically have more scatter than the other material properties. To show the sensitivity of tensile strength, $\sigma_r(\xi = \varepsilon)$ is also plotted for five times and one-fifth the reported tensile strength. For $Y = 16.5$ MPa, the response is elastic–cracked–plastic. For $Y = 3.3$ MPa and 0.66 MPa, the response is elastic–cracked for

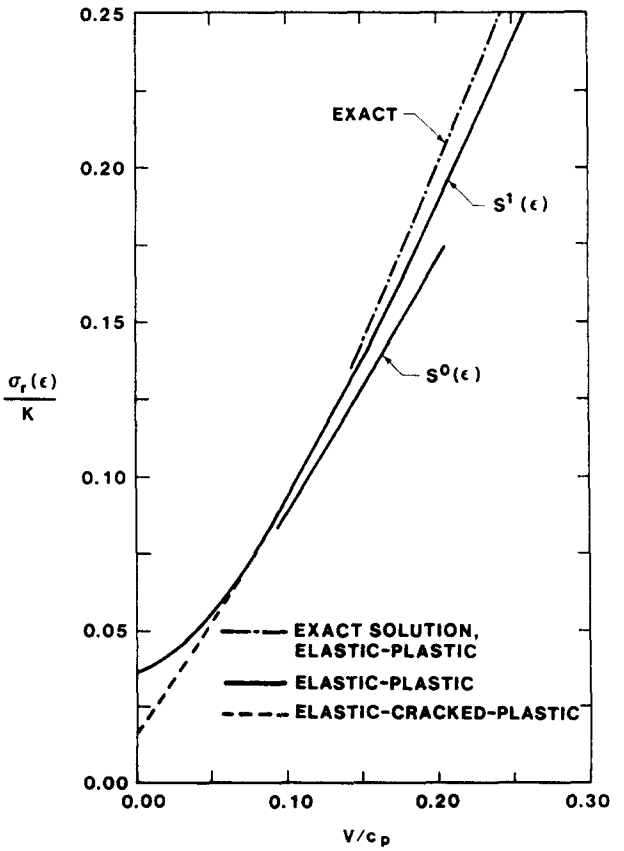

Fig. 3. Radial stress components on the conical nose for Antelope tuff. A comparison of the iterative solutions $S^0(\varepsilon)$ and $S^1(\varepsilon)$ with the exact, nonlinear solution.

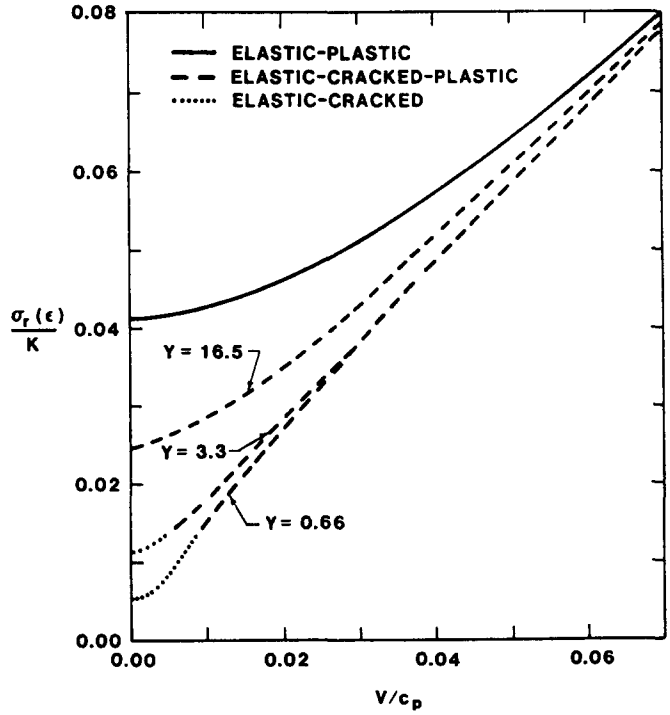

Fig. 4. Radial stress components on the conical nose for Mount Helen tuff. No detectable differences between the iterative solution $S^1(\varepsilon)$ and the exact, nonlinear solution occurred over this range.

$\sigma_r(\xi = \varepsilon)/K < 0.0132$, and elastic–cracked–plastic for $\sigma_r(\xi = \varepsilon)/K > 0.0132$. The dynamic calculations merge to the quasi-static values for V approaching zero.

COMPARISONS WITH FIELD-TEST DATA

As mentioned, penetration, deceleration-time data were obtained for only two, rock targets[7, 8]. These targets were ash-flow and welded tuffs with densities $\rho_0 = 1.62$ and 1.97 Mg m^{-3}, respectively. Post-test, target observations indicated a crater near the target surface that was 1 or 2 nose-lengths deep, followed by a tunnel with about the penetrator diameter. Deceleration-time data[7, 8] show monotonic rises during the crater phase and maxima during the tunnel phase. These cavity-expansion models were developed for the tunnel phase of penetration.

As indicated by eqn (13), axial force on the penetrator nose is proportional to the radial stress on the nose or at the cavity radius. However, another mechanism that increases resistance to penetration is the sliding friction between the penetrator and target material. Most knowledge of friction phenomena at high speeds is for metals and is contained in the article by Bowden and Tabor[19]. This article explains that frictional resistance is controlled by a thin melt layer of material, and post-test observations of penetrators[20] show surface melting of the nose. Coefficient of friction data for steel on steel and steel on nylon show nearly the same resistance which indicates that frictional resistance is dominated by the material with the lower melting point. More recently, Gaffney[21] measured the dynamic friction between rock cores and a rotating steel disc. Data were obtained for velocities to 30 m s^{-1} and contact stresses to 100 MPa. Unfortunately, penetration applications require data for much higher sliding velocities and larger contact stresses. As discussed in [20], the axial resultant force that includes sliding friction is given by

$$F_z = \pi a^2 \sigma_r(\varepsilon)(1 + f/\tan\phi), \tag{34}$$

where the friction coefficient f depends on the penetrator velocity.

Predictions from the theories are now compared with rigid-body penetrator deceleration data. With $\sigma_r(\varepsilon)$ determined from the target motion analysis and eqn (34), deceleration is calculated from

$$dV_z/dt = -F_z/m \tag{35}$$

where m is the penetrator mass and V_z is the penetrator velocity.

For the Antelope tuff ($\rho_0 = 1.62$ Mg m^{-3}) field test[8], the penetrator had total length 1.56 m, aft-body diameter 0.156 m, a 6.0 CRH (caliber radius head) nose shape, and mass 162 kg. The penetrator was propelled with a 0.305 m diameter, smooth-bore, recoilless gun (Davis gun) to an impact velocity of 520 m s^{-1}. Since the penetrator had a smaller diameter than the gun bore, the aft portion of the penetrator was fitted with a foam sabot and a 55.3 kg, steel pusher-plate that fitted the internal diameter of the gun barrel. Gun pressure was applied to the pusher-plate, and the sabot kept the penetrator centered for normal impact. While the foam sabot had negligible mass, the pusher-plate (55.3 kg) added to the effective penetrator mass for the first body-length of penetration. The pusher-plate was eventually stripped from the penetrator near the target surface. Deceleration data with 2 kHz resolution was measured with an on-board accelerometer and digital recording system. The deceleration data shown in Fig. 5 were filtered to 0.5 kHz to remove some higher frequency responses associated with the vibrations of the penetrator and mounting structure for the instrumentation package.

Comparisons of predictions with the deceleration data are also given in Fig. 5. The theoretical model is for a penetrator with a conical nose; whereas, the penetrator used in the field test had an ogival nose. Based on hundreds of full-scale, soil-penetration tests, Young[1] concludes that a 6.0 CRH, ogival nose is nearly equivalent to a conical nose with $\tan\phi = 0.30$. The predictions in Fig. 5 used this equivalent conical nose. Predictions that include sliding friction used

$$f = f_s - (f_s - f_d)(V_z/V_d) \quad \text{for } V_z < V_d \text{ and}$$
$$f = f_d \quad \text{for } V_z > V_d.$$

This relationship is based on the limited data from [19, 21] and used $f_s = 0.50$, $f_d = 0.08$, and $V_d = 30$ m s^{-1}. The predictions also assumed that the pusher-plate was instantly stripped from the penetrator after one body-length of penetration; this accounts for the deceleration jump at $t = 3.0$ ms. At the end of the trajectory, there is another deceleration jump. This sudden jump to zero deceleration occurs because a finite value of radial stress is required

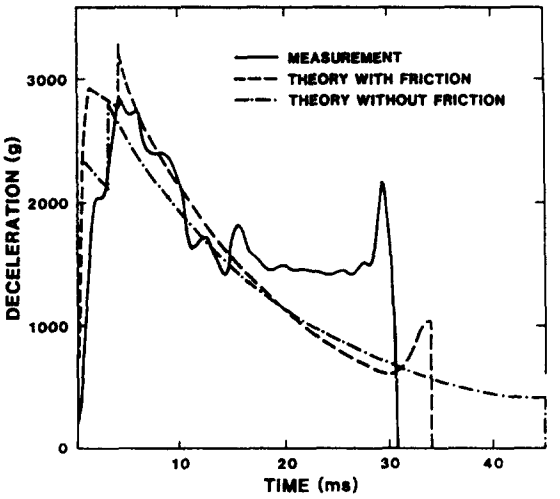

Fig. 5. Deceleration-time predictions and measurement from a field test into Antelope tuff.

to open a cavity. This threshold stress is the quasi-static solution given by eqns (27a, c) and shown in Fig. 3 for V approaching zero. Figure 5 shows predictions that include and neglect the resistance from sliding friction.

For the Mount Helen tuff ($\rho_0 = 1.97$ Mg m^{-3}) field-test[7], the penetrator had total length 1.52 m, aft-body diameter 0.165 m, a 9.25 CRH nose shape, penetrator mass 182 kg, and pusher-plate mass 53.2 kg. The penetrator was accelerated to 411 m s^{-1} impact velocity, and two, on-board accelerometers recorded deceleration. Deceleration-time data filtered to 0.5 kHz and predictions are shown in Fig. 6. Based on the data in [1], the 9.25 CRH nose shape was approximated with a conical nose with $\tan\phi = 0.25$. The prediction with sliding friction used the same relationship as that for Antelope tuff. Figure 6 shows predictions that include and neglect the effect of sliding friction.

DISCUSSION

Research on penetration into geological targets consists of a mix of analytical, experimental, and field-test work. However, this branch of mechanics seems to be dominated by full-scale tests. Over the last two decades, Young[1, 8, 17] and Patterson[7] conducted hundreds of instrumented, full-scale, field-tests into soil, rock, and sea-ice targets. These penetrators usually contained on-board recording systems and measured deceleration during the penetration event. In this study, closed-form solutions for forces on penetrators launched into geological targets have been developed and deceleration-time histories that were in reasonable agreement with field-test measurements predicted. The penetration model was guided by post-test observations that included triaxially sheared material next to the tunnel and radial cracks produced by circumferential tension.

The present models improved our previous work[4, 9] by including three regions of response: a plastic region, a radially cracked region, and an elastic region. In addition, it was discovered that for slow enough penetration velocity, there was the possibility that no plastic region existed. Thus, the elastic–cracked model was developed. Lastly, this study presents accurate, closed-form solutions; whereas, the previous models required the numerical solution of nonlinear, differential equations. These closed-form solutions were programmed for numerical evaluation on a personal computer.

Although the cavity-expansion models were in good agreement with field tests, it is

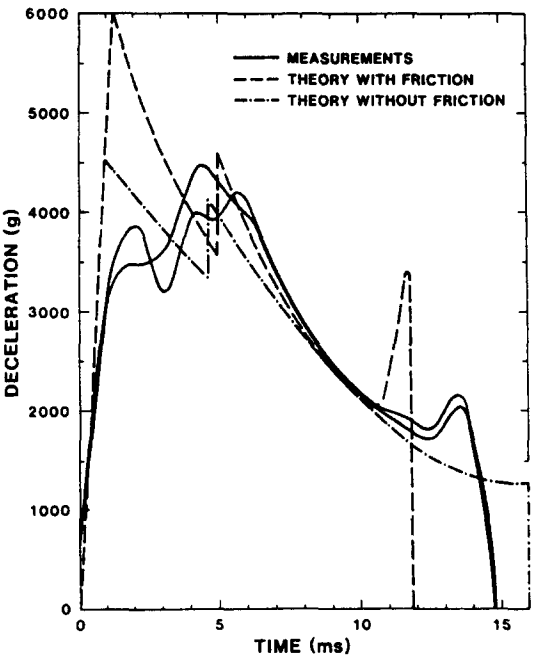

Fig. 6. Deceleration-time predictions and measurements from a field test into Mount Helen tuff.

important to reiterate the major assumptions, which are: (1) the cylindrical, cavity-expansion approximation that considers the target as independent layers normal to the penetration direction and assumes only radial, target motion, (2) a constitutive target description guided by quasi-static data that contains minimum detail, and (3) sliding friction data from experiments very different from those physical situations that occur in penetration events. Clearly, there is a need for additional research in this branch of mechanics.

Acknowledgement—The author thanks Dr. D. B. Longcope of Sandia National Laboratories for many helpful suggestions.

REFERENCES

1. C. W. Young, Depth prediction for earth penetrating projectiles. *J. Soil Mech. Fdns Div. ASCE* **SM3**, 803–817 (1969).
2. R. F. Bishop, R. Hill and N. F. Mott, The theory of indentation and hardness tests. *Proc. phys. Soc.* **53**, 147–155 (1945).
3. Y. M. Ito, R. B. Nelson and F. W. Ross-Perry, Three-dimensional numerical analyses of earth penetration dynamics. DNA 5404F, California Research and Technology, Inc., Woodland Hills, CA 91367 (Jan. 1979).
4. D. B. Longcope and M. J. Forrestal, Penetration of targets described by a Mohr–Coulomb failure criterion with a tension cutoff. *J. appl. Mech.* **50**, 327–333 (1983).
5. R. E. Goodman, *Introduction to Rock Mechanics*. Wiley, New York (1980).
6. M. J. Forrestal and D. B. Longcope, Closed-form solutions for forces on conical-nosed penetrators into geological targets with constant shear strength. *Mech. Mater.* **1**, 285–295 (1982).
7. W. J. Patterson, Sandia National Laboratories, Albuquerque, New Mexico. Letter to P. Hadala, Waterways Experiment Station, Vicksburg, Mississippi (June 1976).
8. C. W. Young, Sandia National Laboratories, Albuquerque, New Mexico. Letter Report on Davis Gun Test TP-3 (R801889) (August 1980).
9. M. J. Forrestal, D. B. Longcope and F. R. Norwood, A model to estimate forces on conical penetrators into dry porous rock. *J. appl. Mech.* **48**, 25–29 (1981).
10. R. Hill, *The Mathematical Theory of Plasticity*. Oxford University Press, London (1950).
11. R. K. Dropek, J. N. Johnson and J. B. Walsh, The influence of pore pressure on the mechanical properties of Kayenta sandstone. *J. geophys. Res.* **83**, 2817–2824 (1978).
12. D. B. Longcope and M. J. Forrestal, Closed-form approximations for forces on conical nosed penetrators into dry porous rock. *J. appl. Mech.* **48**, 971–972 (1981).
13. S. C. Hunter, The propagation of spherically symmetric disturbances in ideally plastic materials. *Proceedings of the Conference on the Properties of Materials at High Rates of Strain*, pp. 147–155. Institute of Mechanical Engineers, London (April 1957).
14. M. J. Forrestal, Forces on conical nosed penetrators into targets with constant shear strength. *Mech. Mater.* **2**, 173–177 (1983).
15. M. J. Forrestal, L. M. Lee, B. D. Jenrette and R. E. Setchell, Gas-gun experiments determine forces on penetrators into geological targets. *J. appl. Mech.* **51**, 602–607 (1984).
16. M. J. Forrestal, F. R. Norwood and D. B. Longcope, Penetration into targets described by locked hydrostats and shear strength. *Int. J. Solids Structures* **17**, 915–924 (1981).
17. C. W. Young and L. J. Keck, An air-dropped sea ice penetrometer. Report SC-DR-71-0729, Sandia Laboratories, Albuquerque, New Mexico (1971).
18. S. W. Butters, H. S. Swolfs and J. N. Johnson, Field, laboratory and modeling studies on Mount Helen welded tuff for earth penetrator test evaluation. DNA 4085F, TerraTek, Salt City, Utah (August 1976).
19. F. P. Bowden and D. Tabor, *The Friction and Lubrication of Solids*, Part 2, Chapter 22. Oxford University Press, London (1968).
20. M. J. Forrestal and D. E. Grady, Penetration experiments for normal impact into geological targets. *Int. J. Solids Structures* **18**, 229–234 (1982).
21. E. S. Gaffney, Measurements of dynamic friction between rock and steel. DNA 4161F, Systems, Science, and Software, La Jolla, CA 92038 (October 1976).